A&A 530, A58 (2011)
DOI: 10.1051/0004-6361/201015419
© ESO 2011

Astronomy & Astrophysics

A close look at the Centaurus A group of galaxies

II. Intermediate-age populations in early-type dwarfs⋆,⋆⋆

D. Crnojević[1,⋆⋆⋆], M. Rejkuba[2], E. K. Grebel[1], G. Da Costa[3], and H. Jerjen[3]

[1] Astronomisches Rechen-Institut, Zentrum für Astronomie der Universität Heidelberg, Mönchhofstrasse 12-14, 69120 Heidelberg, Germany
e-mail: denija@ari.uni-heidelberg.de
[2] European Southern Observatory, Karl-Schwarzschild-Strasse 2, 85748 Garching, Germany
[3] Research School of Astronomy & Astrophysics, Institute of Advanced Studies, Australian National University, Cotter Road, Weston Creek, ACT 2611, Australia

Received 17 July 2010 / Accepted 16 March 2011

ABSTRACT

Aims. We investigate the resolved stellar content of early-type dwarf galaxies in the Centaurus A group, to estimate their intermediate-age population fractions.
Methods. We use near-infrared photometric data taken with the VLT/ISAAC instrument, together with previously analyzed archival HST/ACS data. The combination of the optical and infrared wavelength range permits us to firmly identify luminous asymptotic giant branch stars, which are indicative of an intermediate-age population in these galaxies.
Results. We consider one dwarf spheroidal (CenA-dE1) and two dwarf elliptical (SGC1319.1-4216 and ESO269-066) galaxies that are dominated by an old population. The most recent periods of star formation are estimated to have taken place between ∼2 and ∼5 Gyr ago for SGC1319.1-4216 and ESO269-066, and approximately 9 Gyr ago for CenA-dE1. For ESO269-066, we find that the intermediate-age populations are significantly more centrally concentrated than the predominantly old underlying stars. The intermediate-age population fraction is found to be small in the target galaxies, consistent with fractions of up to ∼15% of the total population. These values might be larger by a factor of two or three, if we considered the observational limitations and recent discussion about the uncertainties in theoretical models. We suggest that there is a correlation between intermediate-age population fraction and proximity to the dominant group galaxy, with closer dwarfs having slightly smaller fractions, although our sample is too small to draw firm conclusions.
Conclusions. Even when considering our results as lower limits, the intermediate-age population fractions for the studied dwarfs are clearly much smaller than those found in similar dwarfs around the Milky Way, but comparable to what is seen for the low-mass M 31 companions. Our results confirm our previous work about early-type dwarfs in the Centaurus A group.

Key words. galaxies: dwarf – galaxies: evolution – galaxies: photometry – galaxies: stellar content – galaxies: groups: individual: CenA group

1. Introduction

The Centaurus A group of galaxies is, together with the more sparse Sculptor group, the nearest prominent galaxy group in the southern sky. At its center is the peculiar giant elliptical galaxy NGC 5128 (=CenA), whose distance is 3.8 Mpc (Harris et al. 2010). Searches for new members of this group were performed by Côté et al. (1997), Banks et al. (1999), and Jerjen et al. (2000). Karachentsev et al. (2002) provided precise radial distance measurements for 17 dwarf members of the group using the tip of the red giant branch (TRGB) method. The current list of members of the CenA group contains 62 galaxies with radial velocities in the Local Group rest frame of $V_{\rm LG} < 550$ km s^{-1} and angular distances from CenA of <30° (Karachentsev et al. 2007).

Apart from the determinations of the individual distances, the study of the resolved stellar populations via deep imaging offers insights in the star formation history (SFH) of these systems. Over the past couple of decades, resolved stellar populations have been studied in most Local Group galaxies in great detail. The main result of all these studies is the surprising variety of their SFHs (see e.g. Grebel 1997; Tolstoy et al. 2009). To explore the role of the environment in the evolution of these systems, it is desirable to investigate the stellar populations and SFHs of dwarf galaxies in an environment that is different from the Local Group. With its higher density of galaxies, the Centaurus A group offers this possibility.

In Crnojević et al. (2010), we considered optical *Hubble* Space Telescope (HST) archival images to perform photometry of six early-type dwarfs in the Centaurus A group, for which the upper part of the red giant branch (RGB) can be resolved. We derived their photometric metallicity distribution functions and looked for stellar spatial gradients in their (predominantly) old populations. Similar work was done for early-type dwarfs in the M 81 group by Lianou et al. (2010). However, we pointed out

⋆ Based on observations collected at the European Southern Observatory, Paranal, Chile, within the observing Programme 073.B-0131.
⋆⋆ Full Table 3 is only available at the CDS via anonymous ftp to cdsarc.u-strasbg.fr (130.79.128.5) or via http://cdsarc.u-strasbg.fr/viz-bin/qcat?J/A+A/530/A58
⋆⋆⋆ Member of IMPRS (International Max Planck Research School) for Astronomy & Cosmic Physics at the University of Heidelberg and of the Heidelberg Graduate School for Fundamental Physics.

Table 1. Fundamental properties of the target dwarf galaxies.

Galaxy	RA (J2000)	Dec (J2000)	T	D (Mpc)	$D_{\rm CenA}$ (kpc)	$E(B-V)$	M_V	$\langle$[Fe/H]$\rangle_{\rm med}$ (dex)	Last SF (Gyr)
CenA-dE1, KK189	13 12 45.0	−41 49 55	−3	4.42 ± 0.33	676 ± 483	0.11	−11.99	−1.52 ± 0.20	∼9
SGC1319.1-4216, KK197	13 22 01.8	−42 32 08	−3	3.87 ± 0.27	198 ± 112	0.15	−13.04	−1.08 ± 0.41	2–5
ESO269-066, KK190	13 13 09.2	−44 53 24	−5	3.82 ± 0.26	113 ± 412	0.09	−13.89	−1.21 ± 0.33	2–3

Notes. The columns are as follows: Col. (1) name of the galaxy; (2–3) equatorial coordinates (J2000, units of right ascension are hours, minutes, and seconds, and units of declination are degrees, arcminutes, and arcseconds); (4) de Vaucouleurs' morphological T-type from Karachentsev (2005); (5) distance of the galaxy derived by Karachentsev et al. (2007) with the TRGB method; (6) deprojected distance of the galaxy from the dominant elliptical CenA (Crnojević et al. 2010); (7) foreground reddening from Schlegel et al. (1998); (8) total absolute V magnitude from Georgiev et al. (2008); (9) photometrically derived median metallicity and intrinsic metallicity dispersion of RGB stars, taken from Crnojević et al. (2010); and (10) epoch of most recent significant star formation episode, as derived in Sect. 4.2.

that optical photometry alone is not enough to unambiguously estimate the fraction of intermediate-age populations (IAPs) in these objects, given the substantial amount of Galactic foreground contamination in the direction of the Centaurus A group. Previous studies have shown that luminous asymptotic giant branch (AGB) stars, indicative of such an IAP, are brighter in the near-infrared (NIR) bands, and that the foreground is easier to separate from the galactic stellar content with this kind of data (e.g., Rejkuba et al. 2006; Boyer et al. 2009). The combination of optical and NIR data is thus a powerful tool to investigate the extent to which and at which ages the target dwarfs produced their IAPs.

Early-type dwarf galaxies of the Centaurus A group have been observed in NIR bands, with the Infrared Spectrometer And Array Camera (ISAAC) at European Southern Observatory Very Large Telescope (ESO VLT). The first results for two early-type dwarf members of this group were presented in Rejkuba et al. (2006). We now study three additional objects of the NIR sample.

The paper is organized as follows. We describe the data in Sect. 2, and present the derived color–magnitude diagrams (CMDs) for both wavelength sets in Sect. 3. The IAPs are then investigated in detail in Sect. 4, and the discussion is presented in Sect. 5. Finally, we draw our conclusions in Sect. 6.

2. Data and photometry

Within the ESO observing programme 073.B-0131, we collected NIR observations of 14 early-type dwarfs in the Centaurus A Group. We choose to study in detail here those galaxies whose stellar content could be fully resolved (thanks to good seeing conditions, i.e. seeing <0.6 arcsec) from these observations, and for which archival HST data were already analyzed by Crnojević et al. (2010), as previously done by Rejkuba et al. (2006).

The sample consists of three objects, namely CenA-dE1, SGC1319.1-4216, and ESO269-066 (in order of increasing luminosity). We report the main properties of the target galaxies in Table 1.

We now separately consider the optical and NIR data for the studied galaxies.

2.1. Optical photometry

The archival optical HST data, taken with the Advanced Camera for Surveys (ACS), were already presented and discussed in Crnojević et al. (2010), and are not described in detail here again. For each of the target galaxies, there is one 1200 s exposure in the $F606W$ filter (roughly corresponding to the V-band) and one 900 s exposure in the $F814W$ filter (corresponding to the I-band). The photometry was performed using the DOLPHOT package (Dolphin 2002), which was also used to estimate photometric errors and observational incompleteness via artificial star tests. Typical photometric errorbars from artificial star tests are shown in the CMDs in Fig. 1. The DOLPHOT package provides in addition magnitudes in the ground-based V- and I-bands, which are those used throughout the paper. The 50% completeness level in the V-band lies in the range ∼27.2–26.8, where the first value refers to the least crowded of the galaxies in this sample, CenA-dE1, and the second to the most crowded, ESO269-066. In the I-band, the 50% completeness ranges from ∼26.6 to ∼26.1. The number of stars in the final photometric catalogs (after quality cuts) is 3675, 26 713, and 39 064 for CenA-dE1, SGC1319.1-4216, and ESO269-066, respectively.

Table 2. NIR imaging observing log.

Galaxy	Date (dd/mm/yy)	F	$t_{\rm exp}$ (s)	AM	Seeing (arcsec)
CenA-dE1	21/04/04	K_S	2352	1.23	0.59
	11/05/04	K_S	2352	1.08	0.34
	27/05/04	K_S	2352	1.21	0.41
	27/05/04	J_S	2100	1.11	0.44
SGC1319.1-4216	14/05/04	K_S	2352	1.44	0.43
	10/07/04	K_S	2352	1.11	0.47
	10/07/04	J_S	2100	1.20	0.77
	19/07/04	J_S	2100	1.32	0.44
ESO269-066	11/05/04	K_S	2352	1.20	0.41
	31/05/04	K_S	2352	1.12	0.34
	31/05/04	J_S	2100	1.21	0.41

Notes. The columns contain: (1) galaxy name; (2) date of observation; (3) filter; (4) exposure time (for the dithered sequences, units of s); (5) airmass (given for the central image in each sequence); and (6) seeing of the combined images (as measured on the combined images, units of arcsec).

2.2. Near-infrared photometry

Deep NIR images of the target dwarfs were taken in service mode with the short wavelength arm of ISAAC NIR array at the VLT at ESO Paranal Observatory. The field of view of the short wavelength arm of ISAAC is 2.5 × 2.5 arcmin^2 and the detector has a pixel scale of 0.148 arcsec. Each galaxy was observed once in the J_S-band by coadding a sequence of dithered short exposures, amounting to a total exposure time of 2100 s per galaxy. K_S-band images were taken with a similar strategy at two different epochs, amounting to a total exposure time of 4704 s per galaxy. The observing log is reported in Table 2.

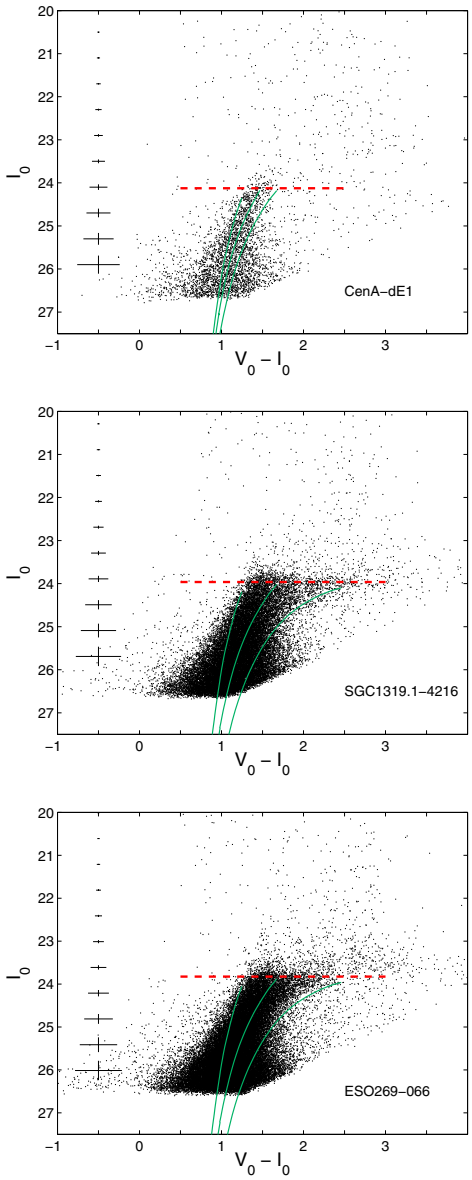

Fig. 1. Optical (dereddened) CMDs of the target galaxies, in order of increasing luminosity. The dominant feature of the CMDs is a prominent RGB, there being a small amount of luminous AGB stars above the TRGB (indicated by a red dashed line). Representative photometric errorbars are plotted at the left side of the CMDs. Green lines are stellar isochrones with a fixed age of 10 Gyr, and varying metallicity: [Fe/H] = −2.5, −1.52, and −1.1 (from the blue to the red side) for CenA-dE1; [Fe/H] = −2.5, −1.08, and −0.4 for SGC1319.1-4216; [Fe/H] = −2.5, −1.21, and −0.4 for ESO269-066 (see text for details).

The standard procedure in reducing IR data was used, and the details of ISAAC data reduction with IRAF[1] are described by Rejkuba et al. (2001). At the end of the reduction, all the images taken in a single dithered sequence were combined. From now on when we refer to an image observed in the J_S-band or K_S-band, we always refer to these combined dithered sequences, and also drop the "s" subscript just using the nomenclature convention J- and K-band.

[1] IRAF is supported by the National Optical Astronomy Observatories, which are operated by the Association of Universities for Research in Astronomy, Inc., under cooperative agreement with the National Science Foundation.

For all the targets, point spread function (PSF) fitting photometry was performed using the suite of DAOPHOT and ALLFRAME programs (Stetson 1987, 1994). The procedure for each galaxy target included the following steps. For each image, we detected all the point sources and determined their PSF using at least 30 relatively bright, non-saturated stars, quite evenly spread across the field. For the observations in both filters, the coordinate transformation were derived. The complete star list was then created from the median-combined image. In case of large variations in seeing between different images, the poorest seeing image was not used in the median combination. PSF fitting photometry using this star list and coordinate transformations was performed simultaneously in each image using ALLFRAME (Stetson 1994). The final photometric catalog for each galaxy contains all the sources that could be measured in both the J-band and at least one K-band image. We apply the following quality cuts to the catalog: the photometric errors (as measured by ALLFRAME) need to be smaller than 0.3 mag in both bands; the sharpness parameter has an absolute value ≤2; and we require $\chi \leq 1.5$. The number of stars from the NIR photometry in each galaxy is: 347 (CenA-dE1), 1505 (SGC1319.1-4216), and 3428 (ESO269-066).

We tied our photometry to the 2MASS photometric system (Carpenter 2001)[2] by matching all the point sources from 2MASS observed in our fields with our J-band and K-band detections (the adopted photometric system is the Vega system). Zero points for each galaxy included thus the correction for the atmospheric extinction. Typically more than seven stars had 2MASS magnitudes, resulting in zeropoint uncertainties of about 0.02 to 0.1 mag in the J-band and 0.03 to 0.15 mag in the K-band.

Completeness and magnitude errors were measured using artificial star tests. Fake stars were added to each image by using its measured PSF and adding the expected noise. Photometry of all the stars was then obtained and typical photometric errors were calculated to be the difference between the input and recovered magnitudes. We also computed the percentage of recovered simulated stars, and tested the extent to which stellar crowding affects the completeness of the observations. CenA-dE1 is the least crowded galaxy of our sample, while ESO269-066 is the most crowded. We chose an elliptical radius that divides the stellar sample into a central subsample (which should be the most affected by crowding) and a subsample containing stars in the outskirts of the galaxies. To define this radius, we used the stellar density profiles computed in Crnojević et al. (2010). CenA-dE1 is off-center in the ISAAC field of view, so we can use the galaxy's limiting (=tidal) radius, beyond which almost only field stars are found. SGC1319.1-4216 and ESO296-066 are more extended than the field of view, so we adopt the half-light radius from Crnojević et al. (2010). The completeness curves are shown in Fig. 2, for both the J- and K-band and for both the central and external stellar subsamples. We fit the curves with the analytic function introduced by Fleming et al. (1995)

$$f = \frac{1}{2}\left[1 - \frac{\alpha(m - m_0)}{\sqrt{1 + \alpha^2(m - m_0)^2}}\right],$$

and overplot the best-fit solutions in Fig. 2. We note that the completeness curves for particularly crowded fields can also be well fitted by alternative analytical functions (e.g., the skewed Fermi law, see Puzia et al. 1999), but the choice of the fitting

[2] http://www.ipac.caltech.edu/2mass/releases/allsky/doc/sec6_4b.html/.

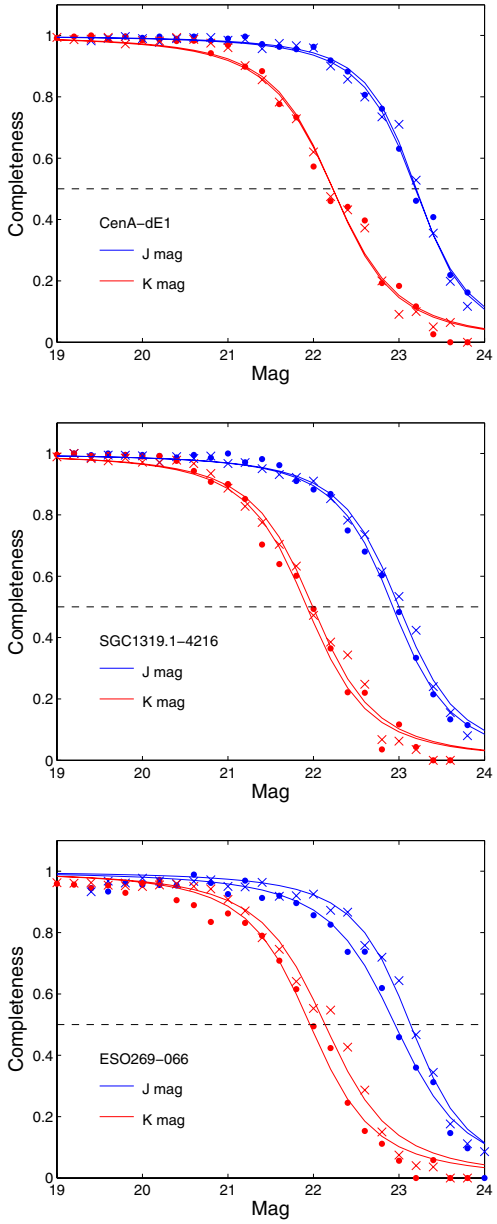

Fig. 2. J- and K-band completeness curves for the target galaxies. The dashed line shows the 50% completeness level. Dots delineate curves computed using stars from the central region of the galaxy, while crosses are for stars located in the outskirts of the galaxy (see text for details). We overplot the best-fitting analytic completeness functions as solid lines (Fleming et al. 1995). Even for the most crowded field (ESO269-066), the inner and outer completeness curves differ very little.

function does not affect our conclusions. Where the crowding is higher, namely for ESO269-066, the completeness does not change significantly as a function of galactic radius. For example, for ESO269-066 the 50% completeness limit (in both bands) is only ∼0.2 mag fainter for the external subsample than for the central one. From now on, we thus assume the completeness to be constant with radius. The photometric errors we derive are shown for each galaxy in the figures of the next section as representative errorbars in the CMDs (they do not include zero point uncertainties).

3. Color-magnitude diagrams

3.1. Optical CMDs

The optical CMDs of the target galaxies are shown in Fig. 1. The data were dereddened taking the Galactic foreground reddening values from the NASA/IPAC Extragalactic Database (NED), which are based on the Schlegel extinction maps (Schlegel et al. 1998). It was assumed that these galaxies do not have a significant internal extinction because of the lack of current star formation. While locally enhanced extinction values might be present (i.e., around dust-obscured carbon-rich AGB stars), this will only affect the individual star itself. We discuss in Sect. 4 the possibility of missing such stars in our sample.

It can be seen that the stellar populations are dominated by a prominent RGB, which is indicative of an old population, but accurate age-dating is not possible because of the metallicity-age degeneracy present in the RGB. The observations reach ∼2.5 mag (I-band) below the tip of the RGB. The latter is computed from the I-band luminosity function using a Sobel edge-detection filter (Lee et al. 1993). We find $I_{0,\mathrm{TRGB}} = 24.13 \pm 0.12$, 23.96 ± 0.13, and 23.83 ± 0.12 for CenA-dE1, SGC1319.1-4216, and ESO269-066, respectively. Unsurprisingly, our results agree with the results of Karachentsev et al. (2007) derived using the same dataset ($I_{0,\mathrm{TRGB}} = 24.18 \pm 0.07$, 23.89 ± 0.04, and 23.86 ± 0.04, respectively).

For the RGB stars, median metallicities and internal metallicity dispersions were derived by Crnojević et al. (2010) assuming that they are mainly old stars ($\gtrsim$10 Gyr). Stellar isochrones from the Dartmouth evolutionary database (Dotter et al. 2008) were used. First, a fixed age of 10 Gyr was assumed and the metallicity varied. For each RGB star located between the TRGB and ∼1 mag below it a metallicity value was interpolated from this grid of isochrones, and a metallicity distribution function derived for the galaxy. In Fig. 1, we overplot three isochrones on each CMD: the first has the lowest metallicity value for that galaxy (corresponding to the lowest metallicity available from the isochrone set), the second represents the median metallicity (also reported in Table 1), and the last the highest metallicity value found.

With the current observations, we can exclude the presence of stars younger than ∼500 Myr in these galaxies (from the absence of an upper main sequence or supergiant stars), but above the TRGB of each galaxy we can see a number of stars that are probably luminous AGB stars. They are the bright tip of the iceberg of an IAP (∼1 to 9 Gyr), which we expect to find at this position for metal-poor stellar populations. For populations more metal-rich than [Fe/H] ~ -1.0, some old and metal-rich stars may also be found above the TRGB, but our target objects are predominantly metal-poor (see Table 1), so we conclude that the presence of these stars is not significant in our sample.

Unfortunately, the low Galactic latitude of the Centaurus A group ($b \sim 20°$) means that a substantial amount of Galactic foreground stars contaminate the CMDs of our target galaxies. We simulate the expected foreground using both the TRILEGAL models (Girardi et al. 2005) and the Besançon models (Robin et al. 2003). An example of the expected contamination in our CMDs is shown in Fig. 3. We plot both optical and NIR CMDs for CenA-dE1, and overplot the positions of foreground stars predicted by the two models (blue crosses for TRILEGAL and red asterisks for Besançon). We convolve the simulated data with photometric errors and take into account incompleteness effects, although we stress that the simulated Galactic stars are only one random realization of the adopted models. For comparison purposes, we plot only stars simulated by Besançon models for star

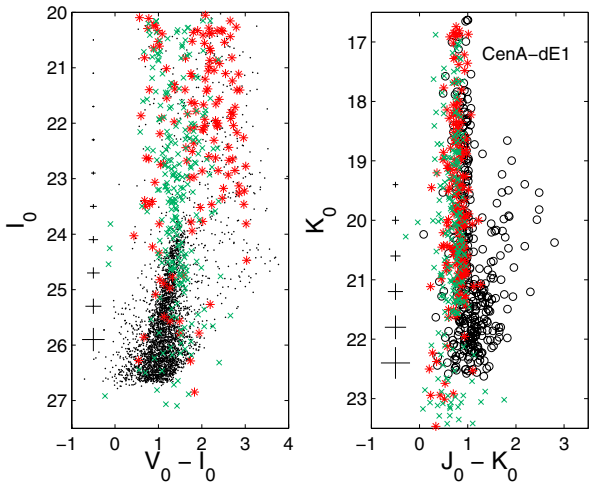

Fig. 3. Optical (*left panel*) and NIR (*right panel*) dereddened CMDs for CenA-dE1. Representative photometric errorbars are plotted on the *left side* of the CMDs. The green crosses represent the Galactic foreground contamination predicted by TRILEGAL models, while the red asterisks are simulated using the Besançon models. The simulated data include corrections for photometric errors and account for incompleteness effects. The models show that the optical CMD is heavily contaminated by foreground objects in the region above the TRGB, while in the NIR CMD is it easier to disentangle foreground stars from the stars belonging to CenA-dE1.

masses >0.15 $M_\odot$, since the TRILEGAL models do not consider these stars in their computation. These few, very low-mass stars if they were indeed to be included would have the effect of extending the Besançon plotted sequence to slightly redder colors. We note that at magnitudes $K_0 \lesssim 20.5$ and colors $J_0 - K_0 \lesssim 1$ (where only foreground stars are found), the number counts resulting from the models are comparable to each other, and similar to the number of observed stars. We stress, however, that the models give slightly different results, and the Besançon model in particular reaches slightly redder colors, although a comparison between the models is beyond the goals of this study. Overall, it is clear from the left panel that the luminous AGB region is the most affected in the optical, and we have no way of determining which stars belong to the dwarf galaxy and which are part of the foreground. We return to the NIR CMD in the following section. In Crnojević et al. (2010), we gave a rough estimate of the possible fraction of the IAP for the target early-type dwarfs by using the fuel consumption theorem (originally introduced by Renzini & Buzzoni 1986; see also Armandroff et al. 1993). We point out that the IAP fractions that we report throughout this work are intended to represent numbers of stars (i.e., the ratio of luminous AGB stars to old RGB stars). The results were the following: for CenA-dE1 and SGC1319.1-4216 the IAP fraction is ∼10%, while for ESO269-066 it is ∼15% of the entire population.

3.2. Near-infrared CMDs

The NIR CMDs are presented in Fig. 4. We corrected the magnitudes for foreground reddening, referring to the NED values derived from the Schlegel extinction maps (Schlegel et al. 1998). For all of the galaxies, the upper part of the RGB is visible at $J_0 \gtrsim 23$ and $K_0 \gtrsim 22$, and the stars above this limit probably belong to the IAPs of these galaxies. We also overplot the 50% completeness limits in all of the panels.

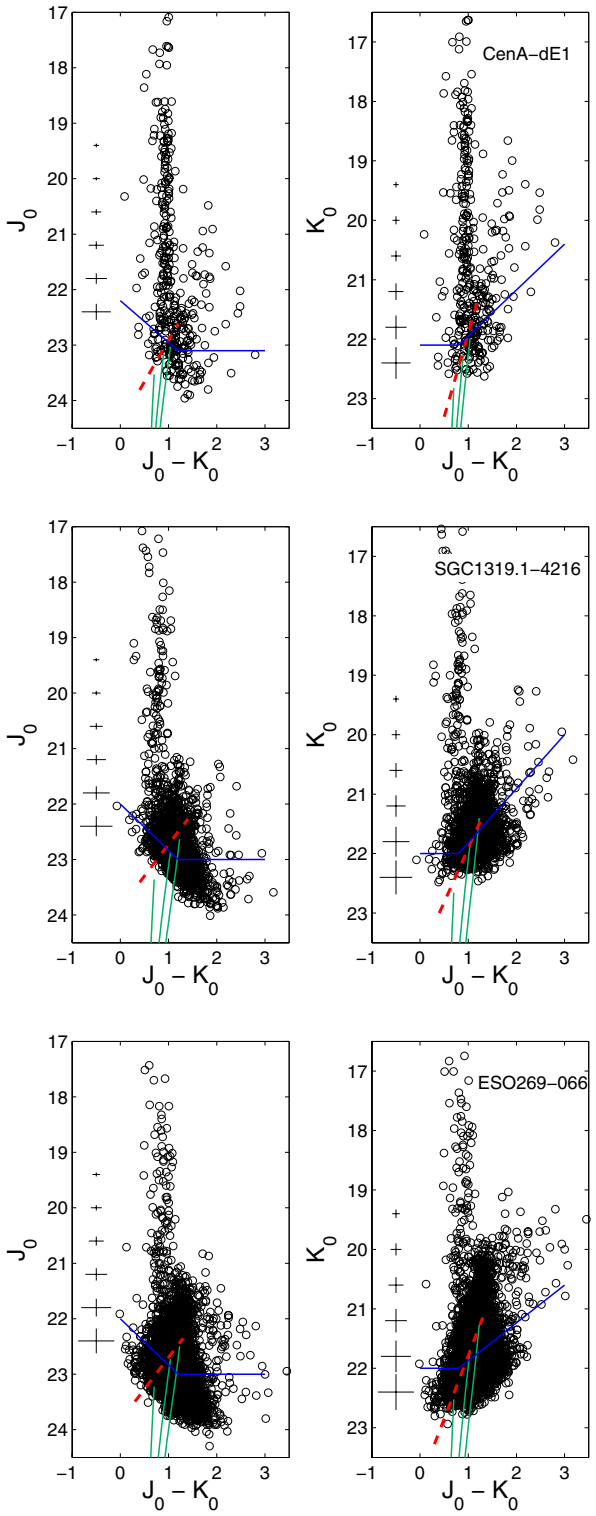

Fig. 4. NIR (dereddened) CMDs of the target galaxies, ordered by increasing luminosity. Representative photometric errorbars are plotted along the CMDs. The red dashed lines indicate the expected position of the TRGB as a function of metallicity (see text for details). The green lines are isochrones with a fixed age of 10 Gyr and spanning the metallicity range of each target galaxy, with the same values as in Fig. 1. The blue solid lines indicate the 50% completeness limits.

We compute the expected TRGB magnitude in both bands using the formulae given in Valenti et al. (2004), assuming the

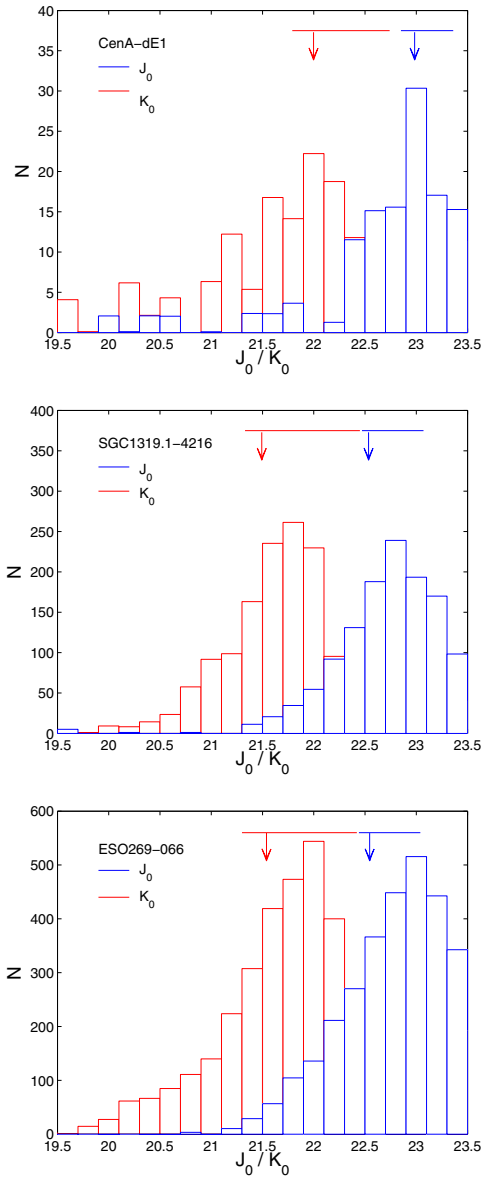

Fig. 5. NIR luminosity functions for the J_0- and K_0-bands of the target galaxies, ordered by increasing luminosity. The numbers have been corrected for Galactic foreground contamination. The arrows indicate the predicted values for the TRGB at the median metallicity of the galaxy, while the horizontal lines above the arrows show the range of predicted TRGB values that stem from the spreads in metallicity (see text for details).

distance moduli derived in the previous section and the median metallicities reported in Table 1. The resulting values are $J_{0,\mathrm{TRGB}} = 22.96 \pm 0.18$, 22.56 ± 0.18, and 22.56 ± 0.18, and $K_{0,\mathrm{TRGB}} = 22.00 \pm 0.18$, 21.50 ± 0.18, and 21.52 ± 0.18 for CenA-dE1, SGC1319.1-4216, and ESO269-99, respectively. We emphasize that the TRGB is not constant as a function of metallicity in these bands, in other words its luminosity depends on the metallicity of the galaxy and all of our targets have a considerable metallicity spread within them. However, as can be seen from the metallicity distribution functions presented in Crnojević et al. (2010), most of the stars in a galaxy have metallicity values around the median value, so that in the luminosity function of the galaxy the approximate locus of the TRGB will still be recognizable as a stellar count decrease toward brighter magnitudes (although not as well a defined one, as would be the case in I-band). We thus check our NIR estimates of the approximate TRGB magnitudes by plotting the luminosity function for both bands in Fig. 5. The luminosity functions were dereddened, and for each magnitude bin the number of predicted Galactic foreground stars from TRILEGAL (similar to that given by Besançon) was subtracted. More precisely, we considered only a fraction of the predicted foreground stars to account for observational incompleteness effects (as a function of magnitude). As an example, for CenA-dE1 in the magnitude bin centered at $K_0 = 21$ the completeness (as derived from artificial star tests) is ∼95%, so we subtract from the dwarf galaxy star counts ∼95% of the simulated TRILEGAL star counts in this magnitude bin. The expected TRGB values derived with the Valenti et al. (2004) formula using the median metallicities are shown in Fig. 5 as arrows, and agree well with the observations. We moreover show a horizontal line including the point of origin of the arrows to indicate the possible range of TRGB values stemming from the range of metallicities, again computed following the Valenti et al. (2004) TRGB calibration equation. For instance, if we use the lowest/highest end of a given galaxy's metallicity range to compute the TRGB with the Valenti et al. (2004) formula, we find a correspondingly fainter/brighter TRGB value. In addition, the NIR CMDs suffer from much larger incompleteness and photometric errors than the optical CMDs, such that the most metal-poor tip of the RGB is fainter than the detection limit in CenA-dE1 and SGC 1319.1-4216, while it is close to the detection limit for ESO269-066. As a reference, in Fig. 4 we also overplot stellar isochrones over the CMDs (as in Fig. 1) to indicate the metallicity range of the galaxies and the shape of the TRGB. We also draw a dashed line passing through the TRGB values computed from the lowest, the median and the highest metallicities found for each galaxy with the Valenti et al. (2004) formula, finding good agreement with the theoretical isochrones.

The NIR CMDs are contaminated by Galactic foreground, but this time the luminous AGB region is not as heavily affected as it is in the optical observations (see right panel of Fig. 3). The vertical feature extending from $J_0 - K_0 \sim 0.3$ to ∼1.0 in Figs. 3 and 4 and over the whole magnitude range is mainly due to Galactic old disk turnoff stars ($J_0 - K_0 \sim 0.36$), Galactic RGB and red clump stars ($J_0 - K_0 \sim 0.65$), and low-mass dwarfs with $M \leq 0.6\ M_\odot$ ($J_0 - K_0 \sim 0.85$, Girardi et al. 2005). That these stars are distributed in vertical sequences is due to the range of distances and luminosities that they span. We now take advantage of the Galactic foreground contamination being more easily recognizable in the NIR CMDs to search for AGB candidates in our galaxies.

3.3. Combined CMDs

Our goal is to use the combined HST/ACS and VLT/ISAAC data to reliably identify candidate AGB stars. To do this, we first cross-correlate the optical and NIR photometric catalogs. The coordinate transformations are initially derived using the IRAF tasks *geomap* and *geoxytran*. The combined catalog was obtained successively with the programme DAOMASTER (Stetson 1987). In Fig. 6, we show the expected location of luminous AGB stars, in both optical and NIR CMDs of CenA-dE1 and SGC1319.1-4216, by overplotting the isochrones from the Padova evolutionary models (Girardi et al. 2010). We point out that some spread of the AGB star magnitudes and colors around the expected positions is due to photometric errors and their intrinsic variability.

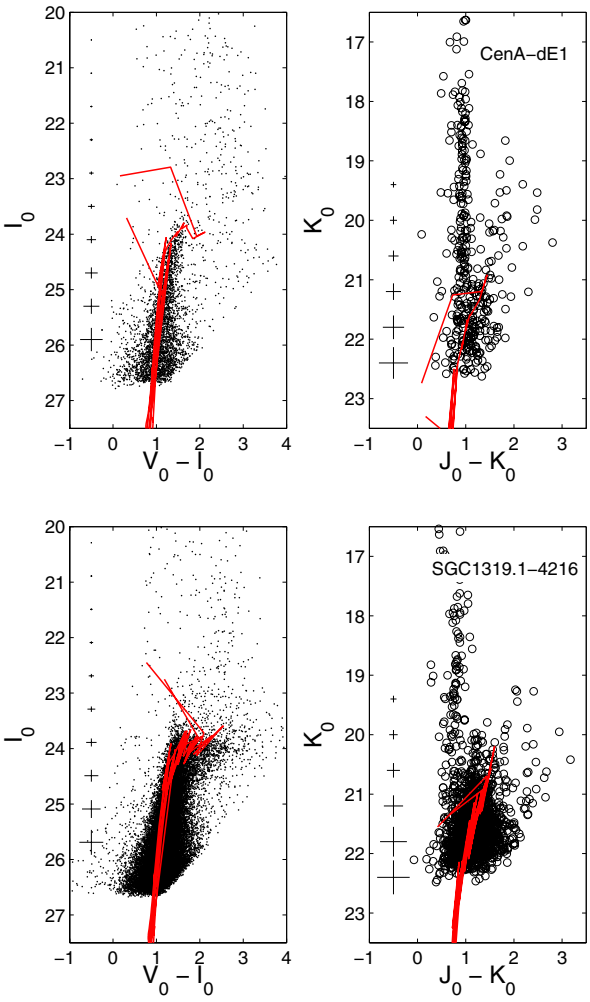

Fig. 6. Optical and NIR (dereddened) CMDs for CenA-dE1 and SGC1319.1-4216. Representative photometric errorbars are plotted along the CMDs. The red lines are isochrones from the Padova evolutionary models with improved AGB phases (Girardi et al. 2010). For CenA-dE1, they have the mean metallicity of the galaxy ([Fe/H] ~ -1.5) and ages of 2 and 9 Gyr; for SGC1319.1-4216, the metallicity is [Fe/H] ~ -1.0 and the ages 2 and 5 Gyr.

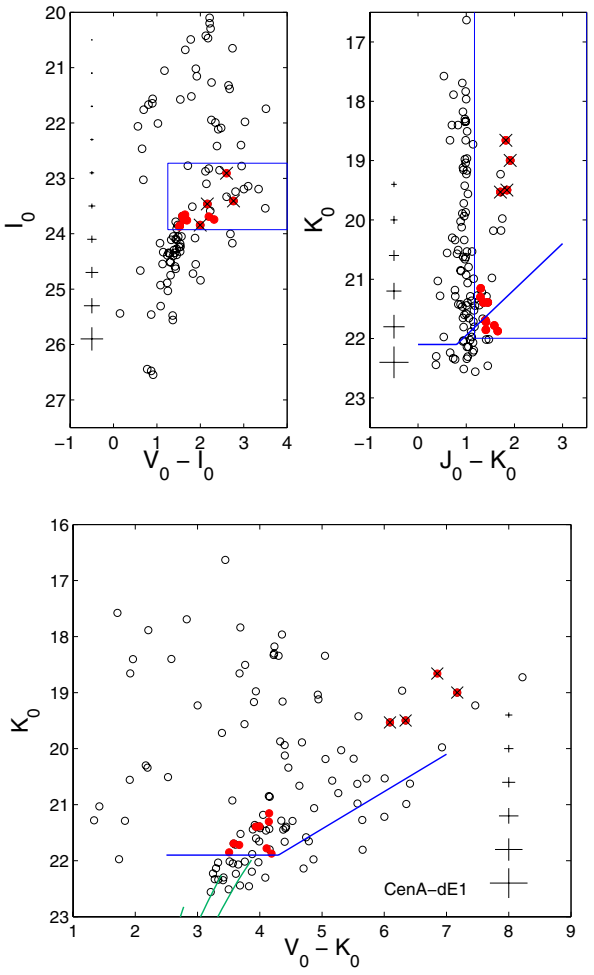

Fig. 7. *Upper panel.* Optical and NIR (dereddened) CMDs for CenA-dE1, showing the stellar point sources cross-identified in both catalogs. Also shown are the boxes used to select luminous AGB candidate stars, and the resulting candidates are plotted as red circles. The objects marked with a black cross are cross-identified in the two datasets, but turn out to be probable background galaxies after visual inspection. Representative photometric errorbars are plotted along the CMDs. The blue solid lines in the NIR CMD indicate the 50% completeness limit. *Lower panel.* Combined CMDs in V_0- and K_0-bands for CenA-dE1. The stellar sources and the symbols are the same as above. We also plot (green lines) the isochrones with a fixed age of 10 Gyr spanning the metallicity range of the galaxy, with the same metallicity values as in Fig. 1. The blue lines have the same meaning as in the *upper panel*.

The combined lists of stars that have both optical and NIR photometry contain 115, 344, and 919 stars, for CenA-dE1, SGC1319.1-4216, and ESO269-066, respectively, and in the upper panels of Figs. 7–9 we show both the optical and the NIR CMDs of the combined list of stars for each of the three galaxies. We note that these numbers are indeed much lower than the numbers of stars found in the optical photometric catalogs alone (see Sect. 2.1). This is partly due to the ISAAC field of view being slightly smaller than the ACS one, and to both the higher resolution and photometric depth of ACS. Unfortunately, this results in a loss of information in the process of cross-correlation, since there might be some mismatches where more than one optical source is found in the vicinity of a NIR source. This is particularly true for SGC1319.1-4216 and ESO269-066, where the stellar density is higher, and from Figs. 8 and 9 we see that the NIR foreground sequences are poorly populated because of these mismatches. To avoid a loss of information for the part of the CMD in which we are most interested, we visually check the positions of the stars that are found within our selection boxes (see below) in both the NIR and optical catalogs, and in this way add a few more matches to our combined catalogs.

On the same CMDs, we also overplot the boxes used in both optical and NIR to select candidate AGB stars. For the optical, the box extends from a magnitude of $I_{0,\mathrm{TRGB}} - \sigma_I$, where σ_I is the observational error at that magnitude (in order not to select RGB stars with erroneously higher magnitudes because of photometric errors), up to $M_I \sim -5.5$. The color range goes from the bluest edge of the TRGB to $V_0 - I_0 \sim 4$ (there are no stars redder than this value). This should be the magnitude range that luminous AGB stars with the average metallicity of the target galaxies cover (see Rejkuba et al. 2006, and references therein). For SGC1319.1-4216 and ESO269-066, we choose to extend the optical selection box based on a few stars with colors $V_0 - I_0 \gtrsim 2.5$ that have magnitudes below that of the TRGB derived from the median metallicity. These stars might belong to the metal-rich population, as the TRGB has slightly fainter magnitudes at higher metallicities (see, e.g., Fig. 1). For the NIR,

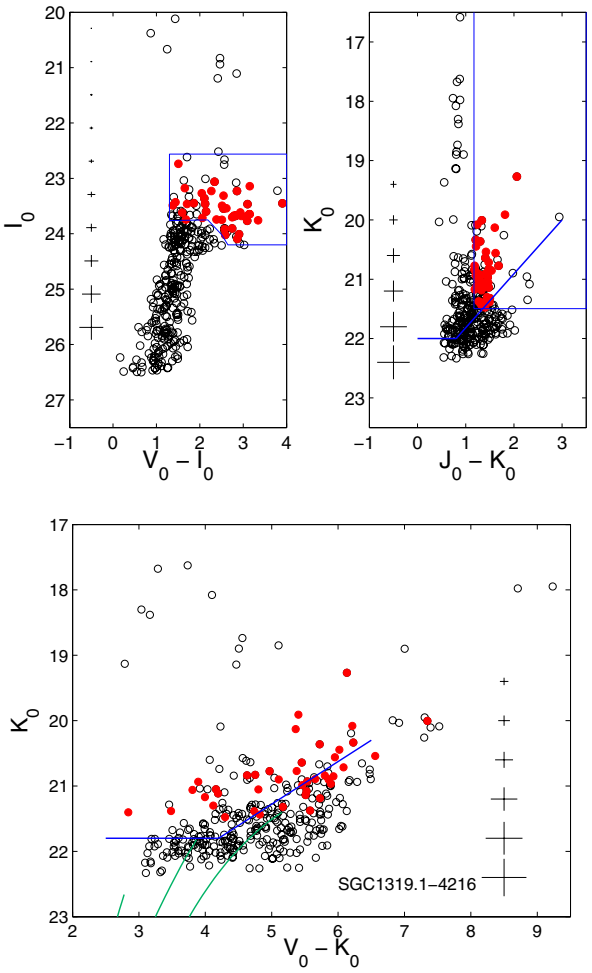

Fig. 8. Same as in Fig. 7, for the galaxy SGC1319.1-4216.

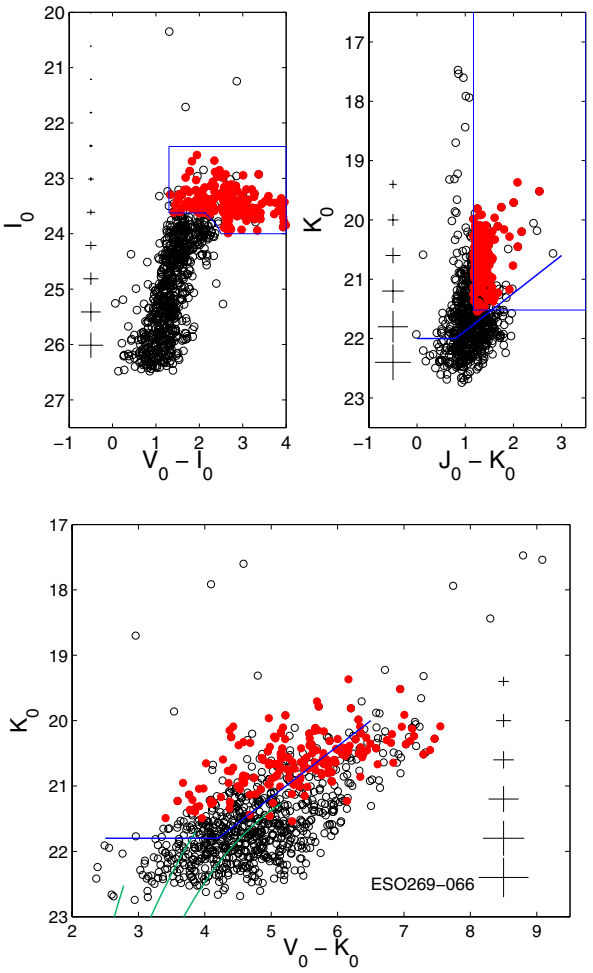

Fig. 9. Same as in Figs. 7 and 8, for the galaxy ESO269-066.

the selection box contains all the stars that are found above the TRGB in these bands, and redwards of the reddest foreground stars of the vertical plume. Our final "AGB candidates" are those stars that are simultaneously found in the optical and the NIR selection boxes, and are plotted in red on these CMDs. We also overplot the 50% completeness limits to the NIR CMDs, to point out that we might be missing the detection of a few luminous AGB stars with colors $J_0 - K_0 \gtrsim 1.0{-}1.5$. This is true in particular for SGC1319.1-4216 and ESO269-066, which have a more metal-rich extension than CenA-dE1. Given the number of stars in the low completeness region, we estimate that there might additionally be at least ∼10 undetected AGB stars for SGC1319.1-4216 and ∼40 for ESO269-066.

There are in total 13 AGB candidates for CenA-dE1, 41 for SGC1319.1-4216, and 176 for ESO269-066. For CenA-dE1, we can see that the four brightest candidates are detached from the rest of the red dots, so we perform a visual inspection of the images and conclude that they are barely resolved background galaxies. In general, the above reported numbers are lower limits to the total number of luminous AGB stars in the target galaxies, given the NIR incompleteness limits.

The lower panels of Figs. 7–9 show the composite $V_0 - K_0$ versus K_0 CMDs for the three studied galaxies. We plot the stars found in the combined lists and mark in red the AGB candidates. To show the expected TRGB position and stress the metallicity spread of these galaxies, we also plot the same isochrones as in Figs. 1 and 4. When looking at the combined CMDs, we note that there are many objects found in the region above the TRGB, but not identified as candidate AGB stars. These sources are mostly foreground contaminants, which are distributed all over the CMDs for these magnitude combinations, but some of them might be unresolved background galaxies. In particular, Saracco et al. (2001) study deep ISAAC observations to derive the number counts of unresolved high-redshift galaxies. From their Fig. 1, we estimate a number of galaxies of up to ∼300 for our field of view, for magnitudes $18 < K_0 < 22$ and distributed on the CMD as shown in their Fig. 3. Owing to the combination of high resolution HST data and excellent seeing ISAAC images, as well as the quality cuts applied to our PSF photometry, most of these galaxies will be rejected from the final combined catalogs, but there is still the possibility of having a few high-redshift and compact contaminants among our AGB candidates, although this cannot be clarified with the current data. The objects found at colors $V_0 - K_0 \gtrsim 8$ are indeed barely resolved background galaxies, as confirmed by visual inspection.

4. Intermediate-age populations

From the combined optical and NIR CMD analysis of the previous section, we are left with nine luminous AGB candidates for CenA-dE1, 41 for SGC1319.1-4216, and 176 for ESO269-066. We report the coordinates and magnitudes of these candidate AGB stars in Table 3 (the complete table is available electronically). These stars belong to the IAP of the target dwarfs,

Table 3. List of the AGB candidates for each galaxy in this study.

Galaxy	ID	α_{2000}	δ_{2000}	J_0	K_0	V_0	I_0
CenA-dE1	168	13 12 46.07	−41 50 53.23	22.60 ± 0.10	21.30 ± 0.07	25.45 ± 0.03	23.76 ± 0.03
	204	13 12 49.83	−41 50 38.48	23.13 ± 0.14	21.72 ± 0.08	25.39 ± 0.03	23.87 ± 0.03
	329	13 12 47.39	−41 50 35.96	22.75 ± 0.10	21.39 ± 0.07	25.33 ± 0.03	23.71 ± 0.03
	...						
SGC1319.1-4216	224	13 22 01.21	−42 32 31.06	22.77 ± 0.10	21.40 ± 0.12	24.24 ± 0.02	22.74 ± 0.02
	517	13 22 01.97	−42 32 15.43	22.88 ± 0.13	21.48 ± 0.12	25.77 ± 0.05	23.71 ± 0.03
	562	13 22 03.12	−42 32 17.90	21.66 ± 0.05	20.45 ± 0.05	26.46 ± 0.06	23.67 ± 0.03
	...						
ESO269-066	919	13 13 10.34	−44 52 49.72	21.82 ± 0.05	20.51 ± 0.03	25.65 ± 0.04	23.47 ± 0.02
	1008*	13 13 11.16	−44 53 30.06	22.23 ± 0.07	20.67 ± 0.05	26.17 ± 0.05	23.61 ± 0.03
	1246	13 13 09.19	−44 53 01.55	22.13 ± 0.07	20.73 ± 0.05	26.29 ± 0.06	23.46 ± 0.02
	...						

Notes. The columns contain: (1) galaxy name; (2) stellar ID from the combined catalog; (3–4) equatorial coordinates (J2000, units of right ascension are hours, minutes, and seconds, and units of declination are degrees, arcminutes, and arcseconds); (5) dereddened apparent J_0-band magnitude; (6) dereddened apparent K_0-band magnitude; (7) dereddened apparent V_0-band magnitude; (8) dereddened apparent I_0-band magnitude. Note that the given photometric errors are the ones resulting from the photometric package. Variable candidates are denoted with an asterisk. For each galaxy, only the first three entries are reported, while the complete table is available from the CDS.

while a few old and metal-rich AGB stars might also be present for SGC1319.1-4216 and ESO269-066, given the red extension of their RGBs. We stress that the old and metal-rich stars in our sample are a very small percentage of the whole luminous AGB population, given the low fraction of stars with [Fe/H] $\lesssim -0.7$. Therefore, in the subsequent analysis, we neglect their contribution, thus assuming that all our AGB candidates belong to the IAP. We now consider their properties in more detail.

With these data, it is in general not possible to firmly separate carbon-rich from oxygen-rich stars among our AGB candidates. However, for these metal-poor galaxies we would expect to find carbon-rich stars at colors $J_0 - K_0 \gtrsim 1.5$ (e.g. Kang et al. 2006 and references therein), and a few stars with these colors are indeed present in all of our target galaxies.

We now verify whether our stellar samples contain dust-enshrouded AGB stars. These objects are extremely faint or undetected in the optical, and very red at NIR wavelengths thus not easily detectable in our J-band data because of incompleteness effects in our observations. For example, van Loon et al. (2005) consider a sample of ∼40 stellar clusters with a range of ages and metallicities in the Small and Large Magellanic Clouds. They find a total of about 30 dust-enshrouded AGB stars in ∼20 young and intermediate-age clusters. These stars are found at $J - K > 2.5$, and have metallicities higher than [Fe/H] = −0.9 dex. However, for clusters with ages and metallicities comparable to our target galaxies, no dust-enshrouded AGB stars were detected. We thus do not expect a significant number of dust enshrouded stars to be present in our target galaxies. We search for stars that have a high quality K-band measurement but no J-band counterpart, and find two such objects in CenA-dE1, none in SGC1319.1-4216 and one in ESO269-066. Of the aforementioned sources, in CenA-dE1 one is found to be slightly outside the limiting radius, while the second is close to the center but has a good measurement only for one of the two K-bands; in ESO269-066, the dust enshrouded candidate also has a low quality measurement in one of the two bands. We thus note that these are candidates but may well be unresolved background galaxies (see previous section).

4.1. Variable candidates

We can also look for additional AGB candidates by considering variability, which is an intrinsic characteristic of luminous AGB stars. For all of the target galaxies, we have at least two observations in the K-band, so we use the difference between the stellar magnitudes at different epochs as a variability indicator. For a long-period variable star, the typical maximum magnitude difference is ∼0.1 to ∼1.5 mag in the K-band, and the period is on the order of $\sim 10^{2-3}$ days (see for example Rejkuba et al. 2003, and references therein). We should thus expect to see variations of a few tens of a magnitude at most, given the observing timescales for our targets (see Table 2).

For CenA-dE1, there are three observations in the K-band because one is a repeated observation. There are 36 days between the first and the last one (see Table 2), which is barely enough to put a lower limit on the number of possible long-period variables. We check whether there are variations between the different K-band observations, but find none. We also verify the whole combined list of sources, looking for stars that display a magnitude variation of more than three times the combined photometric errors in the individual measurements. We find two additional variable sources that lie just below the lower limits of the AGB selection boxes, thus include them in our AGB candidates list. However, when checking them on the images we find that their profiles resemble those of barely resolved background galaxies. In Fig. 10 (upper panel), we display the K-band magnitude difference between the second and the third epochs, since these are the ones with better seeing, for all the candidate AGB stars except one, because it has a low quality measurement in the second K-band observation. We also show (in green) the two likely background galaxies.

The K-band observations of SGC1319.1-4216 were taken 57 days apart, and three of the AGB candidates display variability (blue dots in the central panel of Fig. 10). When considering the entire sample, two stars that lie just leftwards of the NIR selection box, and are found inside the optical selection box, are indeed variables exhibiting a luminosity change by more than 3σ (green symbols). We add the two latter to the number of candidate AGB stars for SGC1319.1-4216 (and report them in the electronic version of Table 3). In this case, one AGB candidate also has a poor quality measurement in the second K-band observation and is thus not shown in the plot.

Finally, for ESO269-066 the timescale for the observations is very short, only 20 days. We are able to see a variability of more than 3σ for only four AGB candidates, as can be seen from the

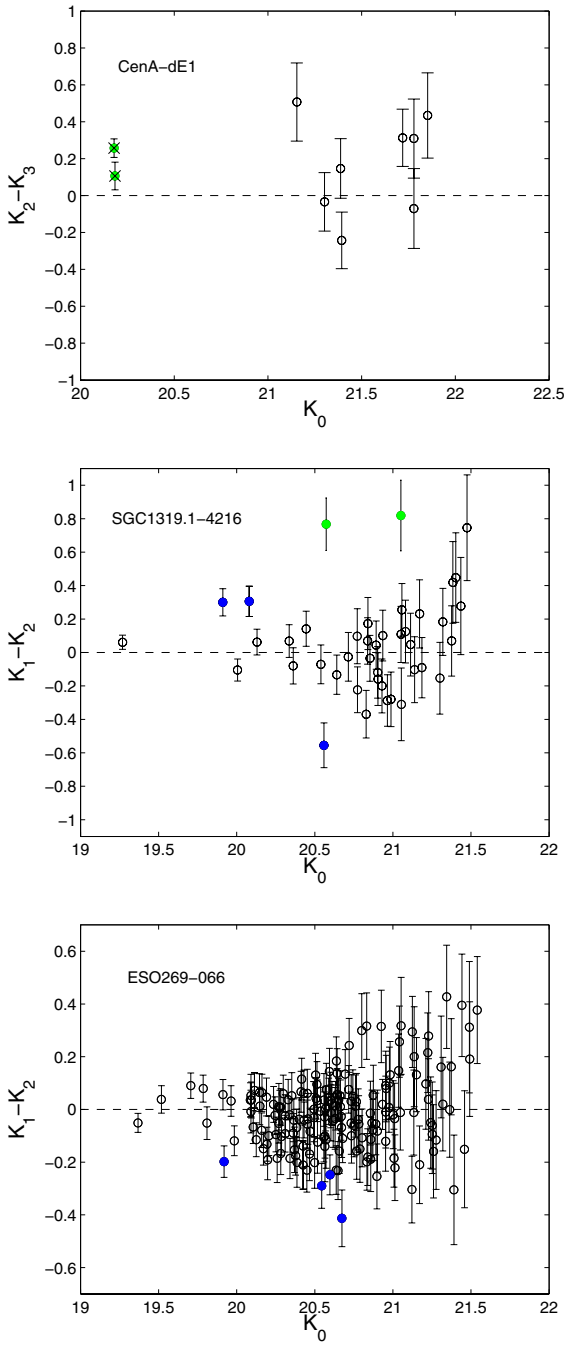

Fig. 10. *K*-band magnitude difference between the first and second observation (or second and third in the case of CenA-dE1), against the combined dereddened *K* magnitude. The target galaxies are ordered by increasing luminosity. We display the magnitude difference for candidate AGB stars, plus for those stars that lie at the edges of the selection boxes but show variability (green dots). For CenA-dE1, the latter turn out to be probable background galaxies after visual inspection and have a black cross on top of the circle (see text for details). Blue objects are AGB candidates for which the magnitude varies by more than three times the combined photometric errors of the individual measurements in the two observations (or in any combination of observations for CenA-dE1). Finally, for both CenA-dE1 and SGC1319.1-4216 one AGB candidate is not shown since it has a poor quality measurement in one of the two plotted *K*-bands.

bottom panel of Fig. 10. No additional variable candidates were found for this galaxy.

4.2. Absolute bolometric magnitudes

We can now use the luminosity of the candidate AGB stars to constrain their ages. This is possible since in this evolutionary stage, at a given metallicity, there is no degeneracy between the position in the CMD of a star and age. In particular, the maximum bolometric luminosity of the AGB candidates can tell us when the most recent episode of star formation took place in a galaxy, with the further advantage that the metallicity dependence of the luminosity is weak compared to the age dependence. We refer in particular to Fig. 19 of Rejkuba et al. (2006), where an empirical relationship is found between age and absolute bolometric magnitude of the tip of the AGB, starting from data for LMC and SMC clusters. Although the bolometric luminosity at the AGB tip also depends on metallicity, this has less of an effect than the age dependence. For example, according to the Padova stellar evolutionary models, at a fixed age (either 2, 4, 6, or 9 Gyr) the difference in bolometric AGB tip luminosity between metallicities of $Z = 0.0006$ (i.e., [Fe/H] = −1.5), $Z = 0.0019$ (i.e., [Fe/H] = −1.0), and $Z = 0.006$ (i.e., [Fe/H] = −0.5) is only ∼0.2 mag.

We thus first compute the bolometric magnitudes of our luminous AGB candidates for each galaxy. We can apply bolometric corrections to both our optical and NIR results, and see whether they give consistent values. Following Rejkuba et al. (2006) (see also their discussion), we adopt NIR bolometric corrections from Costa & Frogel (1996) and optical ones from Da Costa & Armandroff (1990). The results for the three most luminous stars in both optical and NIR wavelengths (which in some cases overlap) are reported in Table 4.

For CenA-dE1, the three most luminous stars in the NIR have absolute bolometric magnitudes of between $M_{\rm bol,\,NIR} \sim -4.1 \pm 0.2$ and $\sim -3.8 \pm 0.2$, while the values derived from the optical are between $M_{\rm bol,\,opt} \sim -4.1 \pm 0.2$ and $\sim -4.0 \pm 0.2$ (with one star in common between the two subsamples). The optical data were taken about 20 days later than the NIR data. We take the average $M_{\rm bol}$ from the three most luminous AGB candidates, which are $M_{\rm bol,\,NIR} \sim -3.9 \pm 0.4$ and $M_{\rm bol,\,opt} \sim -4.1 \pm 0.3$, respectively. When putting these values on the age-absolute bolometric magnitude of AGB tip relation of Rejkuba et al. (2006), we obtain an age of approximately 9.0 ± 1 Gyr for the most recent episode of star formation, indicating that there was very little activity in this galaxy other than at quite old ages.

In SGC1319.1-4216, the three most luminous AGB candidates have $M_{\rm bol,\,NIR}$ between about -5.4 ± 0.5 and $\sim -5.0 \pm 0.3$ and $M_{\rm bol,\,opt}$ between about -4.8 ± 0.2 and $\sim -4.6 \pm 0.2$. Two out of three stars are the same for the two samples, and the optical data were taken between the two *K*-band observations. The average values are $M_{\rm bol,\,NIR} \sim -5.1 \pm 0.6$ and $M_{\rm bol,\,opt} \sim -4.7 \pm 0.3$, respectively. These bolometric magnitudes lead to ages of ∼2.0 ± 1.5 Gyr and ∼5.0 ± 2.0 for the last star formation episode.

Finally, for ESO269-066 the three highest luminosity values in the NIR range from $M_{\rm bol,\,NIR} \sim -5.1 \pm 0.6$ to -5.0 ± 0.3, while in the optical they all are $M_{\rm bol,\,opt} \sim -4.9 \pm 0.2$ (with one star in common out of the three most luminous between the subsamples). This galaxy was observed with HST three months later than in the NIR bands. As before, we compute the average values for the NIR and optical, $M_{\rm bol,\,NIR} \sim -5.1 \pm 0.8$ and $M_{\rm bol,\,opt} \sim -4.9 \pm 0.3$, and derive from these values the time of the most recent episode of star formation, resulting in 2.0 ± 1.5 Gyr and 3.0 ± 1.5 Gyr ago.

We emphasize that we may expect the bolometric values to differ somewhat between the optical and NIR results, given that

Table 4. Magnitudes of the most luminous (in bolometric magnitude) AGB candidates for each galaxy.

Galaxy	ID	I_0	K_0	$V_0 - I_0$	$J_0 - K_0$	$M_{\rm bol,\,opt}$	$M_{\rm bol,\,NIR}$
CenA-dE1	420[a]	23.69 ± 0.03	21.78 ± 0.11	2.20	1.58	−4.14 ± 0.18	−3.24 ± 0.24
	9323[a]	23.74 ± 0.03	21.87 ± 0.20	2.32	1.65	−4.11 ± 0.18	−3.10 ± 0.25
	9248[a,b]	23.66 ± 0.02	21.15 ± 0.08	1.65	1.30	−4.04 ± 0.18	−4.08 ± 0.22
	168[b]	23.76 ± 0.02	21.30 ± 0.07	1.69	1.29	−3.95 ± 0.18	−3.94 ± 0.21
	329[b]	23.71 ± 0.03	21.39 ± 0.07	1.62	1.36	−3.98 ± 0.18	−3.79 ± 0.22
SGC1319.1-4216	224[a]	22.74 ± 0.02	21.40 ± 0.12	1.51	1.36	−4.76 ± 0.17	−3.61 ± 0.28
	1361[a,b]	23.14 ± 0.02	20.08 ± 0.04	3.15	1.24	−4.75 ± 0.17	−5.05 ± 0.27
	1316[a,b]	23.06 ± 0.02	19.27 ± 0.02	2.34	2.06	−4.64 ± 0.17	−5.37 ± 0.48
	1482[b]	23.45 ± 0.02	20.00 ± 0.03	3.90	1.34	−4.63 ± 0.17	−5.03 ± 0.28
ESO269-066	3689[a]	22.58 ± 0.01	20.15 ± 0.04	1.94	1.22	−4.89 ± 0.17	−4.86 ± 0.32
	2139[a]	22.68 ± 0.01	20.24 ± 0.04	2.35	1.31	−4.89 ± 0.17	−4.58 ± 0.34
	4406[a,b]	22.93 ± 0.02	19.99 ± 0.03	3.37	1.17	−4.88 ± 0.17	−5.07 ± 0.32
	3774[b]	22.93 ± 0.02	19.37 ± 0.18	2.60	2.08	−4.70 ± 0.17	−5.13 ± 0.63
	3170[b]	23.21 ± 0.02	19.92 ± 0.03	1.92	1.30	−4.25 ± 0.17	−5.01 ± 0.34

Notes. The columns contain: (1) galaxy name; (2) stellar ID from the combined catalog; (3) dereddened apparent I_0-band magnitude; (4) dereddened apparent K_0-band magnitude; (5) dereddened optical color; (6) dereddened NIR color; (7) absolute bolometric magnitude computed from optical values; and (8) absolute bolometric magnitude computed from NIR values. Note that the combined (ISAAC and ACS) and dereddened NIR and optical magnitudes are given with the photometric errors resulting from the photometric package. [(a)] Among the three most luminous objects in the optical. [(b)] Among the three most luminous objects in the NIR.

the bolometric corrections may have differences from one set of bands to another, and also considering that our sources are possibly long-period variable stars. However, in all cases we find very good agreement between the two datasets. We also point out that the optical bolometric corrections from Da Costa & Armandroff (1990) are based on stars with colors $V - I < 2.6$, so for the three objects in SGC1319.1-4216 and ESO269-066 that have optical colors redder than this limit (see Table 4) the corrections are highly uncertain. We can however see that the resulting absolute bolometric values are consistent with the ones derived starting from the NIR. The bolometric corrections from Costa & Frogel (1996) are instead valid for the entire range of NIR colors spanned by our listed stars. We conclude that while for SGC1319.1-4216 and ESO269-066 the most luminous AGB stars have comparable bolometric luminosities, thus similar ages (with ESO269-066 giving slightly younger values), CenA-dE1 has experienced no significant star formation over the past ∼9 Gyr.

4.3. Spatial distribution

We show the positions of the candidate AGB stars in Fig. 11. The coordinate system is the one of the ISAAC instrument (in pixels), and there is complete overlap with the field of view of ACS since the latter is slightly larger. Red crosses indicate the entire sample of NIR sources (after applying the quality cuts). The AGB candidates are shown as cyan diamonds, while blue filled circles are assigned to candidate variable stars among the AGB stars and green filled circles refer to those stars that are variable but found outside the selection boxes in the CMDs (see previous section). As a reference, we overplot the half-light radius and limiting galactic radius of CenA-dE1 and the half-light radius of SGC1319.1-4216 and ESO269-066, since the last two galaxies extend beyond the field of view covered by the observations (values adopted from Crnojević et al. 2010).

From the previous analysis of HST data (Crnojević et al. 2010), we find that the ratio of AGB/RGB stars remains roughly constant as a function of radius for CenA-dE1 and SGC1319.1-4216, while for ESO269-066 there is an indication that the ratio is slightly higher in the central part of the galaxy. In Fig. 11, we can see that in CenA-dE1 the candidate AGB stars are not symmetrically distributed, and do not tend to cluster in the center of the galaxy. This displacement is probably due to the small number statistics. In SGC1319.1-4216, the luminous AGB stars are smoothly distributed across the galaxy, but mostly found within the half-light radius. Finally, although the AGB candidate distribution for ESO269-066 is similar to that for SGC1319.1-4216, the former has a higher density of AGB candidates in its central part. For the last two galaxies, we note that there are some "holes" in the distribution of the whole stellar sample, but these are due to bright foreground stars. In particular, given the high density of AGB candidates for ESO269-066, these foreground stars might preclude the detection of additional AGB candidates, up to as much as ∼10% of the detected number.

We compare quantitatively the radial distribution of AGB candidates (i.e., the cyan, blue, and green symbols in Fig. 11) to that of RGB stars. For the latter, we select the stars belonging to the RGB from the HST catalog (based on their distribution in the CMD), because they have a broader spatial coverage and are more numerous than the NIR sample. For CenA-dE1, there are too few AGB candidates to enable us to compile these distributions, but we do that for SGC1319.1-4216 and ESO269-066 (Fig. 12). We show the cumulative radial distribution functions (as a function of galactic elliptical radius) for both the AGB and RGB subsamples, and investigate the hypothesis that they come from the same parent distribution with a Kolmogorov-Smirnov test. For SGC1319.1-4216, there is a probability of ∼16% (i.e., less than 2σ significance level) that the two subsamples come from the same parent distribution. The difference in the cumulative distribution functions at a radius of from about 40 to 60 arcsec comes from the asymmetric distribution of AGB candidates, which possibly suggests an off-center star formation activity. On the other hand, for ESO269-066 we can reject the null hypothesis with a probability $\ll$0.1%, which indicates the existence of two statistically separated stellar subpopulations. In Crnojević et al. (2010), we find that a metal-poor and a metal-rich subpopulations among the predominantly old RGB stars are clearly present for this galaxy. This result supports the evidence found in many Local Group early-type dwarfs, that younger and/or more metal-rich subpopulations are more centrally concentrated than the old and/or more metal-poor subpopulations (e.g. Harbeck et al. 2001).

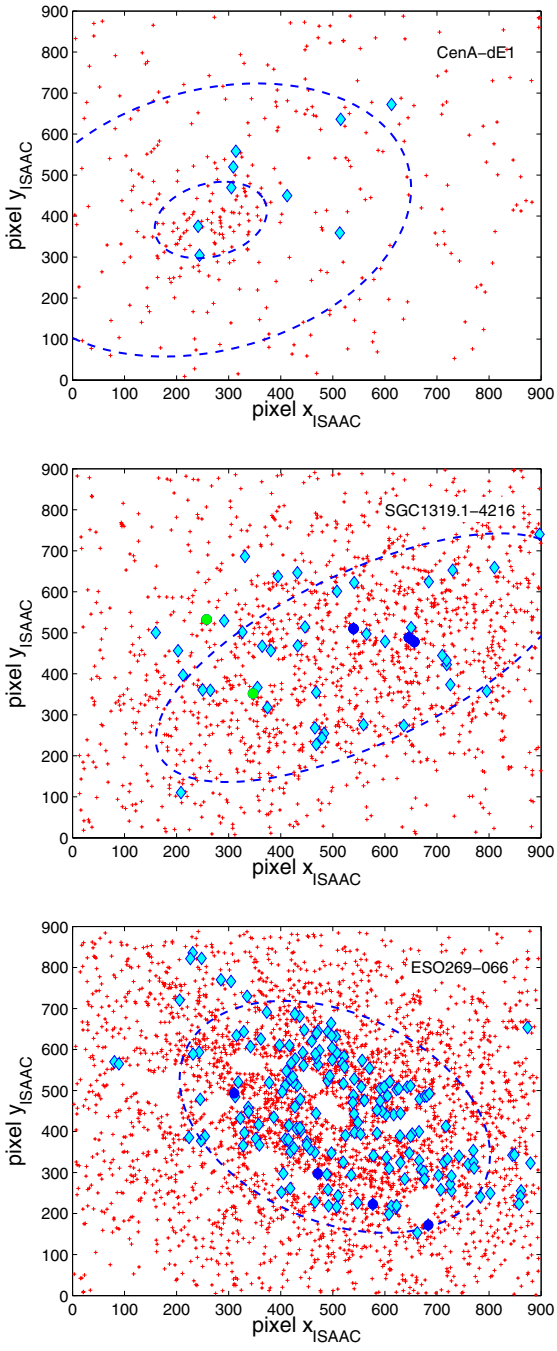

Fig. 11. Stellar positions projected on the sky for the target galaxies (ordered by increasing luminosity). The pixel coordinates refer to the ISAAC field-of-view. Red crosses indicate the NIR sources. The blue dashed lines are, respectively, the half-light radius and the limiting radius for CenA-dE1 and the half-light radius for SGC1319.1-4216 and ESO269-066. Cyan diamonds are candidate AGB stars, blue dots are variable stars among the candidates, and green dots are variable stars found just outside the selections boxes (see text for details). The white "holes" in the distribution of stars for SGC1319.1-4216 and ESO269-066 are due to bright foreground stars that overlap the underlying dwarf galaxy stars.

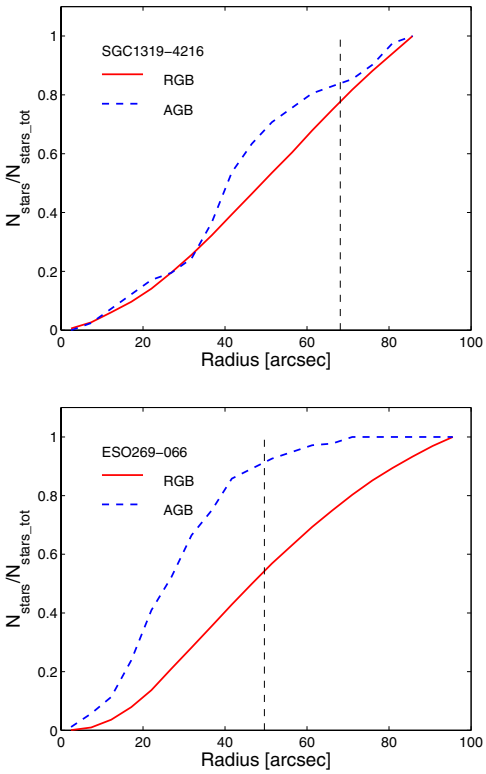

Fig. 12. Cumulative distribution functions of stellar number counts as a function of elliptical radius, for SGC1319.1-4216 and ESO269-066. The different curves show the distribution functions for RGB stars (red line) and candidate AGB stars (blue dashed line, see text for details about the subsamples). The vertical black dashed line indicates the half-light radius, for comparison with Fig. 11 (at these distances, 1 arcsec ~0.02 kpc).

5. Discussion

We now compare our results to those for early-type dwarf galaxies in the Local Group. Among the companions of the Milky Way, there are many objects that show a substantial amount of IAPs (stars with ages in the range ~1–9 Gyr), such as the dwarf spheroidals Fornax, Carina, Leo I, and Leo II (see Grebel & Gallagher 2004 and Table 7 of Rejkuba et al. 2006). The stellar populations of the aforementioned galaxies contain as much as ~50% of IAPs, where these estimates come from detailed SFH recovery from deep CMDs. Among the M 31 companions, the dwarf elliptical galaxies NGC 205, NGC 185, and NGC 147 (e.g., Demers et al. 2003; Nowotny et al. 2003; Davidge 2005) do contain some these IAPs, but among the dwarf spheroidals only AndII and AndVII contain a small fraction of these young populations (Harbeck et al. 2004; Kerschbaum et al. 2004). In dwarf galaxies with more recent star formation, these populations tend to be more centrally concentrated than the older populations (Harbeck et al. 2001).

We note that previous studies have only been able to place upper limits on the HI gas mass of our target galaxies. For example, Bouchard et al. (2007) report values of $M_{\rm HI}/L_B < 0.05, 0.01$, and 0.002 for CenA-dE1, SGC1319.1-4216, and ESO269-066, which are comparable to the values found for Local Group early-type dwarfs with IAPs (see, e.g., Table 1 of Grebel et al. 2003) after considering the lower HI detection limit at the distance of the CenA group. Bouchard et al. (2009) estimates the current rate of star formation (from Hα emission) to be $<0.4 \times 10^{-5}\ M_\odot\ {\rm yr}^{-1}$ for the target galaxies. These results all confirm their previously determined morphological classifications and absence of a significant amount of ongoing star formation.

When considering the bolometric luminosities of the brightest AGB stars of dwarfs in both the Local Group and the

Centaurus A group, with our small data set we can confirm the results of Rejkuba et al. (2006) and conclude that they are all in the same range, with the exception of CenA-dE1, which shows a predominantly old stellar content. The physical properties (total luminosity, mean metallicity, and metallicity dispersion, deprojected distance from dominant group galaxy, see Table 1) of SGC1319.1-4216 and ESO269-066 are indeed very similar to those of Fornax and Leo I, and so are the bolometric luminosities of the brightest AGB stars (e.g., Demers et al. 2002; Menzies et al. 2002; Whitelock et al. 2009; Held et al. 2010), although we have considered dwarf ellipticals, while Fornax and Leo I are dwarf spheroidals. As pointed out by Bouchard et al. (2007), the two CenA group dwarf ellipticals might have been influenced by the radio lobes of CenA, in the sense that their proximity to the giant elliptical might have played a role in the removal of their gas content. However, we stress that only the current deprojected position of these galaxies can be determined, and we have no information about their orbits so that it is difficult to draw any firm conclusion about possible effects such as ram pressure stripping or tidal interactions. CenA-dE1 is on the other hand located further away from CenA (~670 ± 480 kpc, see Table 1) in our sample, and is thus more similar (in distance from the dominant group galaxy, in its luminosity and metallicity content) to the most distant dwarfs of the Local Group. Its last significant star formation episode is significantly older than for the other galaxies and its SFH was most probably much less influenced by the central giant galaxy of the group. The absence of any sizeable IAP younger than 9 Gyr is somehow unexpected in a system as apparently distant from the dominant group galaxy (see, e.g., Bouchard et al. 2009), but Tucana and Cetus in the Local Group show similar characteristics to CenA-dE1 (see, e.g., Monelli et al. 2010). As a reference, we recompute the deprojected distances of the two CenA dwarf companions AM1339-445 and AM1343-452 analyzed in the previous study by Rejkuba et al. (2006). We find a distance from CenA of ~300 ± 330 kpc and ~310 ± 120 kpc, respectively.

5.1. IAP fractions

We estimate the fraction of IAPs with respect to the total stellar content of our target galaxies in the following way. We compute the ratio of the total number of luminous AGB stars, derived in the previous section (also including the variable stars we found outside the selection boxes) to the number of stars found in a box that extends to 0.3 mag below the TRGB in the optical. The latter comprises both old RGB and AGB stars and also a percentage of intermediate-age RGB stars and AGB stars that are still ascending the RGB. Finally, the number of stars in the box extending below the TRGB has been subtracted for expected foreground stars, using TRILEGAL models. The ratio computed in this way is called $P_{\rm IA}$. The values for our target galaxies are ~0.07 for CenA-dE1, ~0.04 for SGC1319.1-4216, and ~0.11 for ESO269-066. We note that SGC1319.1-4216 has a particularly low $P_{\rm IA}$, together with a very wide metallicity spread (see Table 1). SGC1319.1-4216 must have been very active at old ages, before losing its gas reservoir and thus stopping to produce a significant amount of stars. This might be directly linked to a possible tidal interaction with CenA or ram pressure stripping by the intergalactic medium, although the orbits for our target galaxies cannot be constrained, as pointed out above.

The next step to evaluating the IAP fraction is then to consider stellar population models and compare them to our observational findings. We use the Maraston models (Maraston 2005) and follow the procedure of Rejkuba et al. (2006). We first assume that there are two main subpopulations in our galaxies, one that is old (13 Gyr) and the second one with an age of 1, 2, 4, 6, or 9 Gyr (one for each different realization). This is of course a first-order simplification of the true situation, since the star formation might also have proceeded more continuously or in more than two episodes during the galaxies' lifetime. Moreover, we underline that with our data we might be missing a certain amount of IAPs and even younger stars, if we assume that the star formation rate was, in some periods, so low that an observable amount of AGB stars was simply not produced. Thus, once again, we conclude that the fractions we derive are lower limits for the true fractions of IAP.

The model we adopt has a metallicity of [Z/H] = −1.35, which closely matches all of the galaxies in our sample, if we consider that the lifetimes of the AGB phase do not dramatically change as a function of the small differences in metallicity among our target galaxies. We then allow the IAP fraction to vary among the different realizations (from 0 to 1), and each time compute the $P_{\rm IA}$ ratio given by the models. When we compare the results to the observed values found above, we find that CenA-dE1 has an IAP fraction of ~15%; for SGC1319.1-4216, we get an upper limit of only ~5%; while for ESO269-066, the value we find is between ~5% and ~10%. While the empirical relation between age and bolometric luminosity at the AGB tip that we adopt in Sect. 4.2 comes from SMC and LMC clusters (Rejkuba et al. 2006), the metallicity dependence of the luminosity is smaller than our errors in the bolometric magnitudes themselves. The derived ages of our AGB candidates are thus not significantly metallicity dependent, and the assumption of a metallicity [Z/H] = −1.35 for our model will not introduce a bias in our results.

Compared to the rough predictions given in Crnojević et al. (2010) (see Sect. 3.1), the current results are slightly higher for CenA-dE1, and lower for both SGC1319.1-4216 and ESO269-066. We check whether this would change the results about the metallicity content of CenA-dE1, and find that the median metallicity value does not change, while the metallicity spread is smaller by a few percent. For the other two galaxies, there are no significant changes. We emphasize though that recent studies have shown that stellar evolutionary models tend to overpredict the number of luminous AGB stars for dwarfs with low metallicities, similar to our targets, by a factor of as much as ~3−6 (e.g., Gullieuszik et al. 2008; Melbourne et al. 2010). This, together with the arguments mentioned above, reinforces the idea that our results are lower limits to the true IAP fractions in these galaxies.

After computing the IAP fractions, even considering that the real fractions might be twice or three times those derived here, we still can clearly see that they are much lower than the fractions found in similar objects of the Local Group. We note that the relative differences from the Local Group will not be affected by the model uncertainties, since the comparison is observationally based, although the absolute values of both sets might be larger. In particular, we have mentioned that the characteristics of SGC1319.1-4216 and ESO269-066 are similar to those of Fornax and Leo I, but despite this similarity, the recent star formation has proceeded at a much lower rate for the (so far studied) objects in the Centaurus A group. The latter, denser, environment might thus be responsible for the observed properties of its dwarf members. These results again agree with those of Rejkuba et al. (2006), who also found quite low IAP fractions in two dwarf members of this group that resemble the low luminosity companions of M 31. We however stress that the sample is currently too small to draw firmer conclusions, and we would

need to have NIR data also for the other CenA dwarfs with existing optical HST data.

6. Conclusions

We have analyzed archival photometric data of three early-type dwarf galaxies in the Centaurus A group, the dwarf spheroidal CenA-dE1, and the dwarf ellipticals SGC1319.1-4216 and ESO269-066. We have selected the targets based on the availability of both high-resolution HST/ACS data and ground-based VLT/ISAAC data, to analyze the luminous AGB stars in these objects. These stars are useful tracers of IAPs (∼1 to 9 Gyr). From the optical data alone, AGB stars are difficult to separate from the Galactic foreground contamination, by which the Centaurus A group region is affected.

Selecting common stars from the combined optical and NIR CMDs, we have isolated 9 candidate luminous AGB stars for CenA-dE1, 41 for SGC1319.1-4216, and 176 for ESO269-066. To these, we added 2 more stars in SGC1319.1-4216, based on their variability between the sets of K-band observations. We then computed the absolute bolometric magnitudes for the most luminous AGB candidates, and found that they are lower for CenA-dE1, while SGC1319.1-4216 and ESO269-066 have comparable values. We then correlated the absolute bolometric magnitudes to the age of the most recent significant star formation episode in these galaxies. We found a value of 9.0 ± 1.0 Gyr for CenA-dE1, ∼2.0 ± 1.5 to ∼5.0 ± 2.0 for SGC1319.1-4216, and 2.0 ± 1.5 to 3.0 ± 1.5 Gyr for ESO269-066. The two values for SGC1319.1-4216 and ESO269-066 correspond to the different methods of computing bolometric magnitudes, starting from either optical or NIR data, while for CenA-dE1 the two methods give almost identical results.

We find quantitative evidence of two separate subpopulations, namely AGB and RGB stars (i.e., intermediate-age and old subpopulations) for ESO269-066. The AGB subpopulation appears to be more centrally concentrated than the RGB stars, thus resembling similar trends found in Local Group early-type dwarfs. Finally, we estimated the fractions of IAPs of the three target galaxies starting from stellar evolutionary models, and found values of ∼15% for CenA-dE1, an upper limit of only ∼5% for SGC1319.1-4216, and a value between ∼5% and ∼10% for ESO269-066. These are likely to be lower limits to the true fractions.

When comparing our results to dwarf galaxies of the Local Group, we clearly see that despite having similar physical properties and positions within the two groups, the objects in the Centaurus A group tend to have a lower IAP fraction than observed in the dwarf spheroidal companions of similar luminosity of the Milky Way. Our results are comparable to those found for low-mass dwarf spheroidal companions of M 31. We suggest that this difference might be due to environmental effects, which lead to the loss of the neutral gas content for the dwarfs in this dense group, and preferentially for objects that are closest to the dominant elliptical CenA. However, we stress that our sample, together with the study of Rejkuba et al. (2006), consists of only five galaxies, so these are just preliminary findings. Finally, we underline that this kind of study has just begun for dwarf galaxies outside the Local Group and that there is need for more observational data.

Acknowledgements. We thank an anonymous referee who helped to improve the paper. We thank the service mode support at Paranal for conducting the near-infrared observations. D.C. acknowledges financial support from the MPIA of Heidelberg, as part of the IMPRS program, and from the Astronomisches Rechen-Institut of the University of Heidelberg. D.C. is thankful to S. Pasetto and S. Jin for enlightening conversations and support. This publication made use of data products from the Two Micron All Sky Survey, which is a joint project of the University of Massachussetts and the Infrared Processing and Analysis Center/California Institute of Technology, funded by the National Science Foundation. This work is also based on observations made with the NASA/ESA *Hubble* Space Telescope, obtained from the data archive at the Space Telescope Science Institute. STScI is operated by the Association of Universities for Research in Astronomy, Inc. under NASA contract NAS 5-26555. This research made use of the NASA/IPAC Extragalactic Database (NED), which is operated by the Jet Propulsion Laboratory, California Institute of Technology, under contract with the National Aeronautics and Space Administration.

References

Armandroff, T. E., Da Costa, G. S., Caldwell, N., & Seitzer, P. 1993, AJ, 106, 986
Banks, G. D., Disney, M. J., Knezek, P. M., et al. 1999, ApJ, 524, 612
Bouchard, A., Jerjen, H., Da Costa, G. S., & Ott, J. 2007, AJ, 133, 261
Bouchard, A., Da Costa, G. S., & Jerjen, H. 2009, AJ, 137, 3038
Boyer, M. L., Skillman, E. D., van Loon, J. T., Gehrz, R. D., & Woodward, C. E. 2009, ApJ, 697, 1993
Carpenter, J. M. 2001, AJ, 121, 2851
Costa, E., & Frogel, J. A. 1996, AJ, 112, 2607
Côté, S., Freeman, K. C., Carignan, C., & Quinn, P. J. 1997, AJ, 114, 1313
Crnojević, D., Grebel, E. K., & Koch, A. 2010, A&A, 516, A85
Da Costa, G. S., & Armandroff, T. E. 1990, AJ, 100, 162
Davidge, T. J. 2005, AJ, 130, 2087
Demers, S., Dallaire, M., & Battinelli, P. 2002, AJ, 123, 3428
Demers, S., Battinelli, P., & Letarte, B. 2003, AJ, 125, 3037
Dolphin, A. E. 2002, MNRAS, 332, 91
Dotter, A., Chaboyer, B., Jevremović, D., et al. 2008, ApJS, 178, 89
Fleming, D. E. B., Harris, W. E., Pritchet, C. J., & Hanes, D. A. 1995, AJ, 109, 1044
Georgiev, I. Y., Goudfrooij, P., Puzia, T. H., & Hilker, M. 2008, AJ, 135, 1858
Girardi, L., Groenewegen, M. A. T., Hatziminaoglou, E., & da Costa, L. 2005, A&A, 436, 895
Girardi, L., Williams, B. F., Gilbert, K. M., et al. 2010, ApJ, 724, 1030
Grebel, E. K. 1997, in Rev. Mod. Astron., ed. R. E. Schielicke, 10, 29
Grebel, E. K., & Gallagher, III, J. S. 2004, ApJ, 610, L89
Grebel, E. K., Gallagher, III, J. S., & Harbeck, D. 2003, AJ, 125, 1926
Gullieuszik, M., Held, E. V., Rizzi, L., et al. 2008, MNRAS, 388, 1185
Harbeck, D., Grebel, E. K., Holtzman, J., et al. 2001, AJ, 122, 3092
Harbeck, D., Gallagher, III, J. S., & Grebel, E. K. 2004, AJ, 127, 2711
Harris, G. L. H., Rejkuba, M., & Harris, W. E. 2010, PASA, 27, 457
Held, E. V., Gullieuszik, M., Rizzi, L., et al. 2010, MNRAS, 404, 475
Jerjen, H., Binggeli, B., & Freeman, K. C. 2000, AJ, 119, 593
Kang, A., Sohn, Y., Kim, H., et al. 2006, A&A, 454, 717
Karachentsev, I. D. 2005, AJ, 129, 178
Karachentsev, I. D., Sharina, M. E., Dolphin, A. E., et al. 2002, A&A, 385, 21
Karachentsev, I. D., Tully, R. B., Dolphin, A., et al. 2007, AJ, 133, 504
Kerschbaum, F., Nowotny, W., Olofsson, H., & Schwarz, H. E. 2004, A&A, 427, 613
Lee, M. G., Freedman, W. L., & Madore, B. F. 1993, ApJ, 417, 553
Lianou, S., Grebel, E. K., & Koch, A. 2010, A&A, 521, A43
Maraston, C. 2005, MNRAS, 362, 799
Melbourne, J., Williams, B., Dalcanton, J., et al. 2010, ApJ, 712, 469
Menzies, J., Feast, M., Tanabé, T., Whitelock, P., & Nakada, Y. 2002, MNRAS, 335, 923
Monelli, M., Hidalgo, S. L., Stetson, P. B., et al. 2010, ApJ, 720, 1225
Nowotny, W., Kerschbaum, F., Olofsson, H., & Schwarz, H. E. 2003, A&A, 403, 93
Puzia, T. H., Kissler-Patig, M., Brodie, J. P., & Huchra, J. P. 1999, AJ, 118, 2734
Rejkuba, M., Minniti, D., Silva, D. R., & Bedding, T. R. 2001, A&A, 379, 781
Rejkuba, M., Minniti, D., Silva, D. R., & Bedding, T. R. 2003, A&A, 411, 351
Rejkuba, M., Da Costa, G. S., Jerjen, H., Zoccali, M., & Binggeli, B. 2006, A&A, 448, 983
Renzini, A., & Buzzoni, A. 1986, in Spectral Evolution of Galaxies, ed. C. Chiosi, & A. Renzini, Astrophysics and Space Science Library, 122, 195
Robin, A. C., Reylé, C., Derrière, S., & Picaud, S. 2003, A&A, 409, 523
Saracco, P., Giallongo, E., Cristiani, S., et al. 2001, A&A, 375, 1
Schlegel, D. J., Finkbeiner, D. P., & Davis, M. 1998, ApJ, 500, 525
Stetson, P. B. 1987, PASP, 99, 191
Stetson, P. B. 1994, PASP, 106, 250
Tolstoy, E., Hill, V., & Tosi, M. 2009, ARA&A, 47, 371
Valenti, E., Ferraro, F. R., & Origlia, L. 2004, MNRAS, 354, 815
van Loon, J. T., Marshall, J. R., & Zijlstra, A. A. 2005, A&A, 442, 597
Whitelock, P. A., Menzies, J. W., Feast, M. W., et al. 2009, MNRAS, 394, 795